ACS APPLIED MATERIALS & INTERFACES

Research Article

Cite This: ACS Appl. Mater. Interfaces 2019, 11, 22561−22574

www.acsami.org

Ion Gel Dynamic Templates for Large Modulation of Morphology and Charge Transport Properties of Solution-Coated Conjugated Polymer Thin Films

Erfan Mohammadi,[†] Chuankai Zhao,[†] Fengjiao Zhang,[†,∥] Ge Qu,[†] Seok-Heon Jung,[‡] Qiujie Zhao,[§] Christopher M. Evans,[§] Jin-Kyun Lee,[‡] Diwakar Shukla,[†] and Ying Diao*[,†]

[†]Department of Chemical and Biomolecular Engineering, [§]Department of Materials Science and Engineering, University of Illinois at Urbana−Champaign, Urbana, Illinois 61801, United States

[‡]Department of Polymer Science & Engineering, Inha University, Incheon 402-751, South Korea

Supporting Information

ABSTRACT: Dynamic surfaces play a critical role in templating highly ordered complex structures in living systems but are rarely employed for directing assembly of synthetic functional materials. We design ion gel templates with widely tunable dynamics (T_g) to template solution-coated conjugated polymers. We hypothesize that the ion gel expedites polymer nucleation by reconfiguring its surface to facilitate cooperative multivalent interactions with the conjugated polymer, validated using both experimental and computational approaches. Varying ion gel dynamics enables large modulation of alignment, molecular orientation, and crystallinity in templated polymer thin films. At the optimal conditions, ion-gel-templated films exhibit 55 times higher dichroic ratio (grazing incidence X-ray diffraction) and 49% increase in the relative degree of crystallinity compared to those templated by the neat polymer matrix. As a result, the maximum hole mobilities increase by factors of 4 and 11 along the $\pi-\pi$ stacking and the backbone directions. Intriguingly, we observe a synergistic effect between the gel matrix and the ionic liquid that produces markedly enhanced templating effect than either component alone. Molecular dynamics simulations suggest that complementary multivalent interactions facilitated by template reconfigurability underlie the observed synergy. We further demonstrate field-effect transistors both templated and gated by ion gels with average mobility exceeding 7 $cm^2\ V^{-1}\ s^{-1}$.

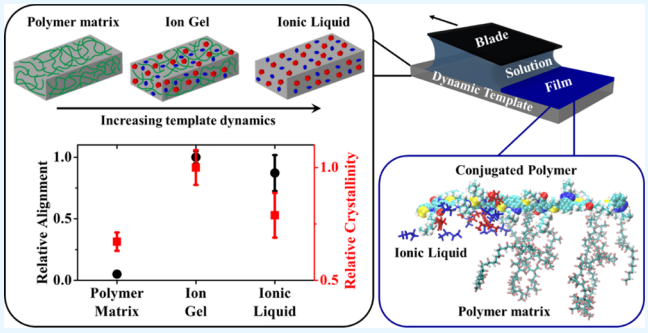

KEYWORDS: *conjugated polymer, printed electronics, solution coating, responsive surfaces, dynamic templates, morphology control, ion gel*

INTRODUCTION

Solution-processable semiconducting polymers received an upsurge of interest during recent years given their wide range of potential applications in printed electronics, energy-harvesting/storage devices, and chemical, mechanical, and biological sensors.[1,2] It has been widely reported that the electronic characteristics of conjugated polymers are highly sensitive to morphological parameters across all length scales.[3−8] Therefore, various approaches have been used to control multiscale morphology such as versatile meniscus-guided coating (MGC) techniques,[9−17] molecular design strategies,[18,19] and substrate surface treatments.[17,20−27] Understanding the role of surfaces in directing conjugated polymer assembly is particularly important. In contrast to conventional bulk polymer processing from the melt, conjugated polymers are usually solution-cast on substrates to form thin-film devices. Previous studies have identified the importance of specific substrate−polymer interactions,[26,27] substrate−polymer lattice matching (epitaxy),[28] surface energy,[17,29,30] and topology[20−22] to controlling the morphology of conjugated polymer thin films. However, the role of substrate dynamics is rarely studied or exploited. In fact, prior works on surface-directed assembly of conjugated polymers have almost exclusively focused on static, rigid surfaces, whose templating effects are usually weak for structurally complex macromolecular systems that exhibit large degrees of disorder and conformation dynamics. Among the few dynamic substrates reported are viscoelastic polymer surfaces[31] and liquid surfaces.[32−35] It has been shown that by controlling polymer dielectric surface viscoelasticity, crystalline grain size in vapor-deposited pentacene thin films can be significantly modulated.[31] Moreover, nonvolatile liquid substrates were employed as passive free surfaces to facilitate processing of aligned conjugated polymer thin films.[32−35] We also reported ionic-

Received: February 15, 2019
Accepted: June 5, 2019
Published: June 5, 2019

DOI: 10.1021/acsami.9b02923
ACS Appl. Mater. Interfaces 2019, 11, 22561−22574

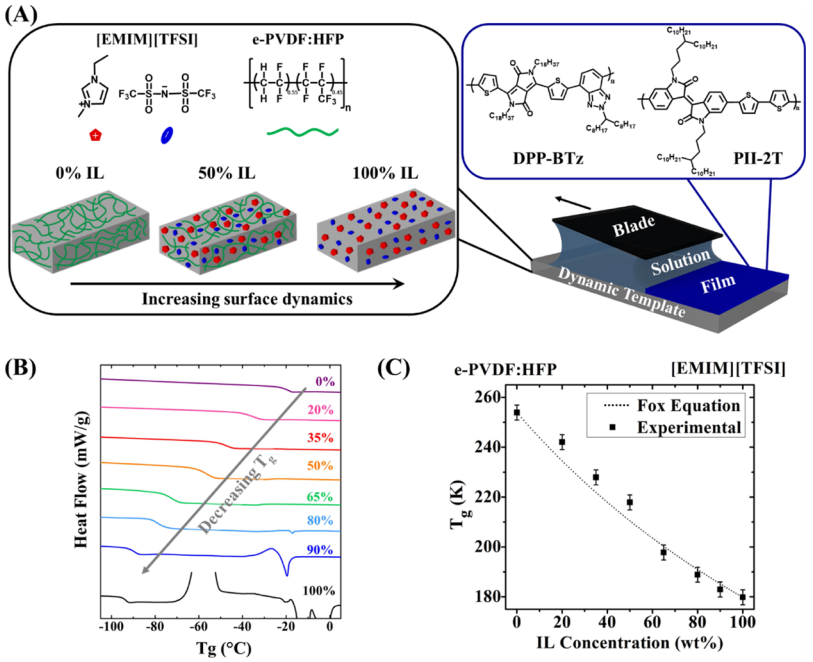

Figure 1. Ion gel dynamic templates of tunable dynamics for semiconducting polymer solution coating. (A) Schematic (not to scale) of MGC on the ion gel dynamic template. The arrow indicates the coating direction. Molecular structures of [EMIM][TFSI] IL, e-P(VDF:HFP) polymer matrix, and conjugated polymers (DPP-BTz and PII-2T) are depicted. The ion gel composition is tuned from 0 to 100% in terms of IL wt % shown in the inset. (B) Representative DSC traces as a function of IL wt % in the ion gel templates. All templates exhibited a single T_g within the temperature range scanned, and the data were recorded during the second heating cycle after removing prior thermal history in the first cycle. (C) Influence of IL content on the glass-transition temperature of the templates compared to the "Fox equation". The Fox equation relates ion gel T_g at a specific composition of w_{IL} (IL wt %) and $w_{polymer}$ (polymer wt %) to their T_g values in pure phases ($T_{g,IL}$ and $T_{g,polymer}$) through the following relation: $T_g = \left(\frac{w_{IL}}{T_{g,IL}} + \frac{W_{polymer}}{T_{g,polymer}}\right)^{-1}$.

liquid (IL)-infused nanoporous surfaces that can reconfigure their surface structure so as to expedite crystallization and assembly of conjugated polymers during MGC.[15] However, liquid surfaces do not offer adjustable surface properties for systematic modulation of multiscale morphology critical to establishing the structure−property relationship. Overall, there are rarely any general approaches that can systematically modulate the morphology of conjugated polymers across all length scales during solution printing and coating.

In our recent work, we demonstrated the concept of dynamic templating for directed assembly of conjugated polymers using IL-infused nanoporous surfaces, which are compatible with solution coating and printing.[15] We showed that the IL can self-optimize its interactions with conjugated polymers by rearranging its surface structure to reveal favorable binding sites. Such template reconfigurability markedly enriches the conjugated polymers near the template and can potentially expedite polymer crystallization and assembly.

In this work, we first report polymer gels as dynamic, reconfigurable templates for directing multiscale assembly of conjugated polymers during MGC. Dynamic templates are defined as surfaces that promote crystallization by reconfiguring their surface to enhance interactions with the assembling media. Gel-based dynamic templates offer widely tunable template dynamics (esp. the glass-transition temperature) by varying the liquid-to-polymer matrix ratio. Specifically, we construct an ion gel composed of an IL and a physically cross-linked polymer matrix as dynamic templates. Ion gels can further serve as a high-capacitance dielectric in transistor devices. By tuning the ion gel dynamics, we are able to drastically modulate conjugated polymer in-plane alignment, crystallinity, and out-of-plane orientation. The compound effect of these enhanced morphological characteristics led to an order of magnitude increase in the carrier mobility measured in the field-effect transistor (FET) geometry. Surprisingly, we observe a synergistic effect between the IL and the gel matrix, which led to an exceptional polymer chain alignment and crystallinity, outperforming the neat IL and the gel matrix. On the basis of our molecular dynamics (MD) simulation studies, we attribute this synergistic phenomenon to the complementary multivalent interactions of the IL and polymer matrix with the conjugated polymer: while IL cations interact with the conjugated backbone, the polymer matrix preferentially interacts with the nonpolar alkyl side chains. We hypothesize that these complementary multivalent interactions, facilitated by rapid template reconfigurability, enhance conjugated polymer crystallization by lowering the nucleation barrier. Although ion gels have been extensively studied as high-capacitance dielectric layers for thin-film transistors (TFTs), they have not been used for large modulation of conjugated polymer morphology before. We further demonstrate the bifunctionality of the ion gel as both the dynamic template and the high-capacitance dielectric to attain high-performance organic TFT devices.

RESULTS

Dynamic Template Fabrication and Characterizations. On the basis of our previous work,[15] 1-ethyl-3-methylimidazolium bis(trifluoromethylsulfonyl)imide ([EMIM][TFSI]) can effectively template the crystallization of two donor−acceptor (D−A) conjugated polymers because of fast reconfigurability of its ions and strong ion−π

DOI: 10.1021/acsami.9b02923
ACS Appl. Mater. Interfaces 2019, 11, 22561−22574

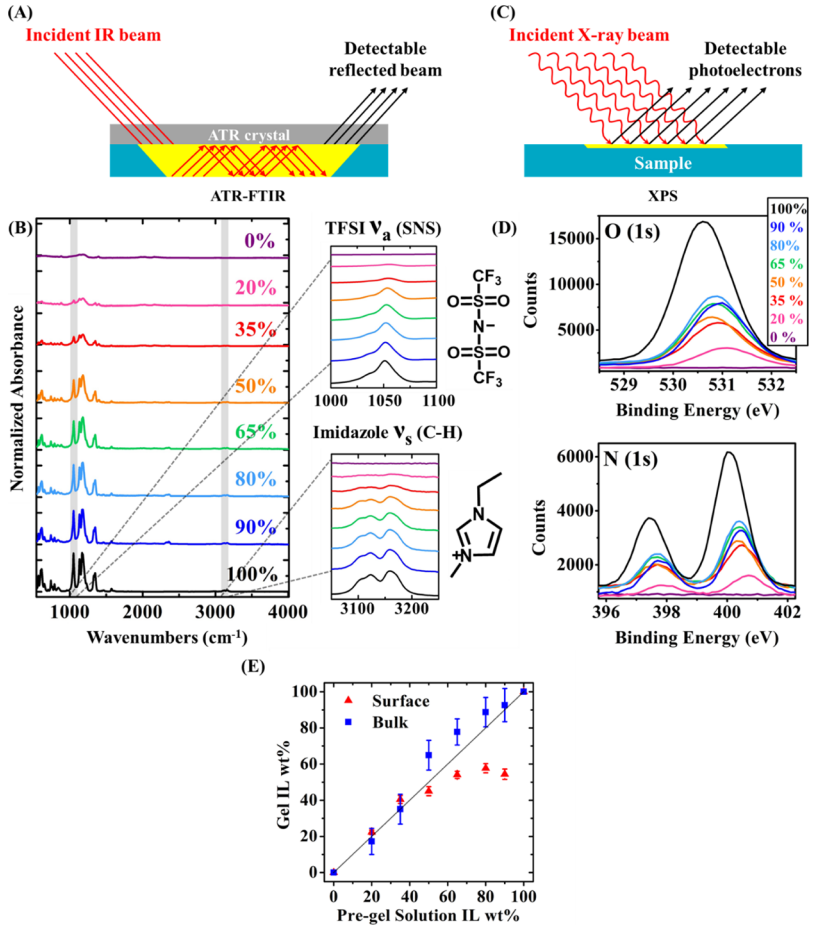

Figure 2. Characterization of ion gel bulk vs surface composition. (A) Schematic of ATR−FTIR spectroscopy and (B) absorbance spectra of ion gels as a function of pregel IL wt %. In the inset, the peaks ascribed to IL's anion (SNS antisymmetric vibration at W = 1025−1075 cm^{-1}) and cation (C−H vibration of the imidazolium ring at W = 3100−3170 cm^{-1}) are depicted, which were used to estimate the IL content in the bulk ion gel. (C) Schematic of XPS and (D) high-resolution spectra of the O (1s) and N (1s) regions as a function of pregel IL wt %. (E) Estimated gel IL wt % in the bulk vs surface. Ion gel's bulk composition is comparable to that of the pregel solution, while the surface (in vacuum) is enriched with the e-P(VDF:HFP) polymer matrix.

interactions. Therefore, [EMIM][TFSI] was employed as the IL for ion gel fabrication in this work. For the polymer matrix, we chose elastic polyvinylidene fluoride-*co*-hexafluoropropylene (e-P(VDF:HFP)) with a 55:45 VDF to HFP molar ratio and a low glass-transition temperature (T_g) of around −20 °C. e-P(VDF:HFP) was previously used as a high-capacitance dielectric layer in FETs[36] and also as a dynamic polymer matrix for ion-gel-based self-healing ionic conductors.[37] Ion gels were prepared by dissolving both the IL and the polymer matrix in a cosolvent (acetone), and the resulting solution was spin-cast on glass or silicon substrates (see the Experimental Section). The thickness of resulting ion gel films was within the 1−2 μm range.

Two high-performing solution-processable D−A polymers were selected for this study. We chose a high-performing diketopyrrolopyrrole-benzotriazole (DPP-BTz)[12,18] copolymer as the main system and tested the generality of our observations using an isoindigo-*alt*-bithiophene-based polymer (PII-2T).[15,17] We deposited conjugated polymer thin films from chloroform (CF) solution on ion gel templates via MGC, which mimics the physics of roll-to-roll printers (Figure 1A). We verified experimentally that [EMIM][TFSI], e-P(VDF:HFP), and their ion gels are practically immiscible with the polymer ink solution during fast MGC. The composition of the ion gels varied from 20 to 90 wt % IL in order to establish the relationship between template properties, conjugated polymer thin-film morphology, and charge transport properties.

To evaluate template composition-dependent bulk dynamics, we carried out differential scanning calorimetry (DSC) to obtain bulk glass-transition temperatures (T_g(b)). T_g for amorphous polymer films thicker than ∼100 nm is very similar to T_g(b)[38] and quantifies the ensemble-averaged polymer chain segmental dynamics and ionic motion. The resulting DSC thermograms are shown in Figure 1B. The T_g of e-P(VDF:HFP) (0 wt % IL) was measured as ∼−20 °C, consistent with the previous report,[36] and the T_g of neat [EMIM][TFSI] (100 wt % IL) was determined to be −93 ± 3 °C, also consistent with the literature.[39,40] Progressively increasing the IL content of the ion gel from 0 wt % monotonically decreases the T_g(b), thereby increasing the template dynamics possibly through enhancing the segmental motion of the polymer matrix (Figure 1C). The measured T_g(b) followed the prediction of the Fox equation[41] very well (dashed line in Figure 1C). We acknowledge that the surface glass-transition temperature (T_g(s)) can substantially deviate from T_g(b), specifically in the presence of conjugated polymer solution, yet it remains challenging to measure T_g(s) directly.

DOI: 10.1021/acsami.9b02923
ACS Appl. Mater. Interfaces 2019, 11, 22561−22574

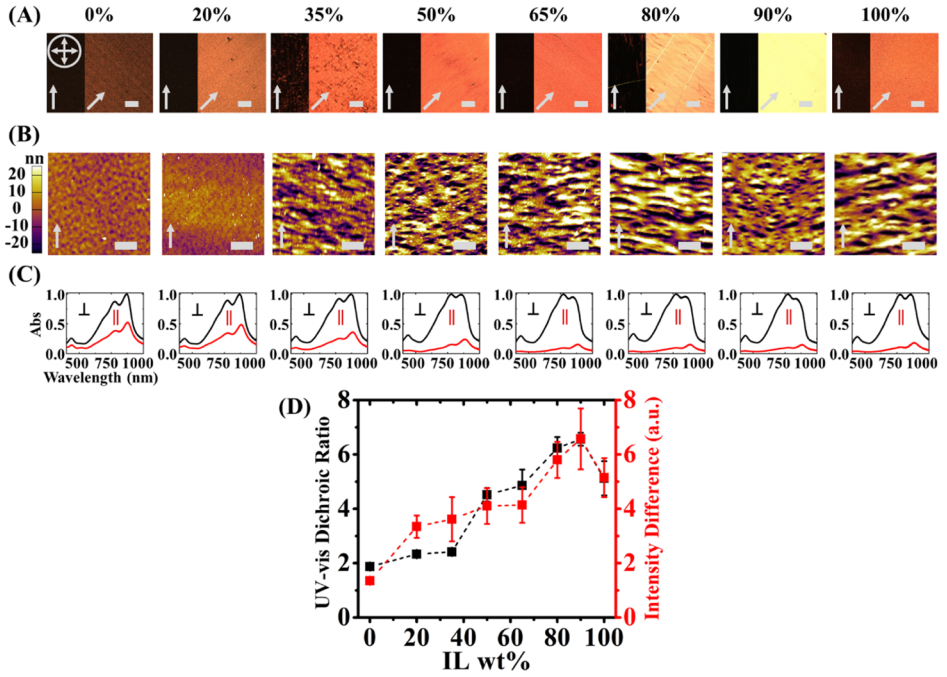

Figure 3. Macro- and mesoscale morphology of DPP-BTz films coated on various dynamic templates. (A) C-POM images. The orientation of crossed polarizers is denoted as crossed arrows, and the single arrow shows the coating direction. All scale bars are 100 μm. With increasing IL content in the template, stronger birefringence effect is observed in templated DPP-BTz thin films. Upon rotation, the whole C-POM image uniformly varies in intensity, which indicates that the film is highly aligned at the macroscale. (B) Tapping-mode AFM height images with 2 μm scale bars, showing increase in domain size with the increase of IL content in the template. (C) Normalized absorption spectra of polarized UV−vis spectroscopy, where the sign ∥ (⊥) denotes the film orientation when the coating direction is parallel (perpendicular) to the axis of the polarizer. (D) Polarized UV−vis dichroic ratio (black) and C-POM intensity difference (red) as a function of the IL content in the template. The birefringence is calculated as the difference between the average intensities when the film is oriented 45° vs 0° with respect to the polarizer axis (Figure 3A). Error bars were obtained from at least 10 measurements on each sample.

Nonetheless, we expect T_g(s) to follow the same trend as T_g(b) across the template series.[31,42]

Next, we characterized the bulk and surface chemical composition of ion gel films by attenuated total reflectance Fourier transform infrared (ATR−FTIR) spectroscopy (Figure 2A,B) and X-ray photoelectron spectroscopy (XPS) (Figure 2C,D), respectively. ATR−FTIR spectra normalized with the radiated volume (depth of penetration ∼2 μm) are summarized in Figure 2B, showing a monotonic increase in the intensity of IL characteristic absorption peaks with increasing IL content in the pregel solution. Two regions are magnified in the inset: the peaks at the 3100−3170 cm^{-1} wavenumber range correspond to C−H vibration in the cation imidazole ring and signals at 1010−1080 cm^{-1} are attributed to anion SNS antisymmetric vibrations.[43] There are clear peak shifts in both selected regions (Figure S1) because of the change in chemical environments of corresponding vibrations, suggesting strong interactions between the IL and the polymer matrix. We analyzed peak areas in both regions to quantify the actual IL content in the ion gel film and found that it is comparable to the IL content in the pregel solution (Figure S2). To further determine the surface composition of ion gels, we carried out XPS (penetration depth <10 nm) which measures the surface elemental composition of ion gels in vacuum. From high-resolution XPS spectra of O (1s), N (1s), and S (2p) core-level signals (Figures 2D and S3), we estimated the surface IL content summarized in Figure 2E. This result indicates that the surface composition of the ion gels is comparable with the bulk composition at low to medium pregel IL content of ≤50 wt % but deviates from the bulk composition when the pregel IL content exceeds 50 wt % (Figure S4). Specifically, the gel IL content plateaus at ∼60 wt % despite continuous increase of pregel IL concentration; such surface enrichment of e-P(VDF:HFP) may be related to the minimization of surface energy because of lower surface energy of the polymer matrix compared to that of the IL. Similar to FTIR chemical shifts, XPS binding energies varied with the pregel IL content, suggesting significant interactions between [EMIM][TFSI] and eP(VDF:HFP) at the ion gel surface (Figure S5). It should be noted that XPS measurements were performed under high vacuum ($P < 1 \times 10^{-9}$ Torr). Given the dynamic properties of ion gel templates, we expect the ion gel surface composition to change upon exposure to the ink solution during MGC, shown via contact angle measurements below.

To further investigate ion gel interfacial properties during MGC, solvent (CF) dynamic contact angle measurements were carried out on various templates, revealing rapid adaptability of IL-rich templates (80 and 90 wt %) to CF exposure. Figure S6A,B summarizes the time-dependent contact angle measurements, suggesting that polymer-rich (<50 wt % of IL) and IL-rich (≥50 wt % of IL) templates exhibit two different evaporation behaviors. Droplet evaporation on polymer-rich templates occurred initially at constant wetting radius (R_w) with pinned triple-phase contact line, followed by moving contact line mode featuring constant contact angle (θ) and decreasing R_w. Toward the end of droplet evaporation, both θ and R_w decrease with the moving contact line. In contrast, for IL-rich templates, only pinned contact line mode was observed. The CF droplet on neat IL

DOI: 10.1021/acsami.9b02923
ACS Appl. Mater. Interfaces 2019, 11, 22561−22574

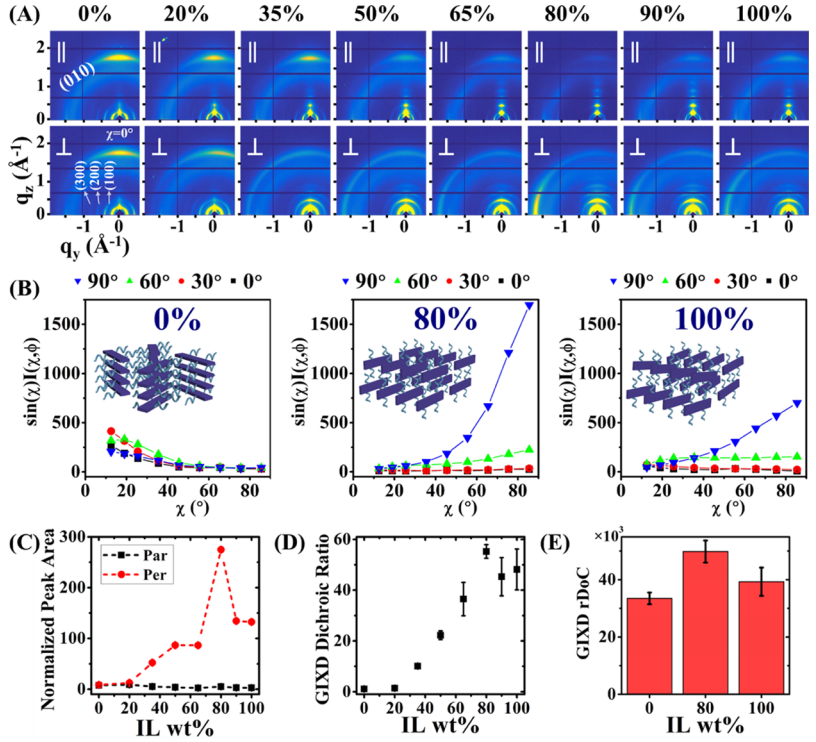

Figure 4. Quantification of DPP-BTz molecular packing, orientation, and crystallinity via GIXD. (A) GIXD patterns for films coated on various templates, measured with the incidence beam parallel and perpendicular to the coating direction above the critical angle. (B) Normalized intensity of the DPP-BTz $\pi-\pi$ stacking (010) peak as a function of polar angle χ and substrate in-plane rotation angle φ for films deposited on templates with 0, 80, and 100% IL; the films were transferred to OTS-treated SiO_2 prior to the measurement. Data were acquired at various in-plane rotation angles of the substrate: φ = 0° (parallel), 30°, 60°, and 90° (perpendicular) in terms of the coating direction relative to the incident beam. Peak intensities were normalized by the exposure time and the irradiated volume to allow direct comparison among various films. Insets illustrate the inferred crystallite orientation. (C) Normalized edge-on $\pi-\pi$ stacking peak area as a function of gel IL wt % for scans parallel and perpendicular to the coating direction. (D) GIXD dichroic ratio as a function of IL content in the template calculated from $R = \frac{A_{Per}}{A_{Par}}$, where A_{Per} (A_{Par}) is the normalized area of edge-on $\pi-\pi$ stacking peak perpendicular (parallel) to the coating direction. (E) rDoC obtained by integrating the $\pi-\pi$ stacking peak intensity over χ and φ for templates with 0, 80, and 100 wt % IL. Error bars are due to the standard errors of (010) peak areas from multipeak fitting.

showed a unique evaporation behavior with very low contact angle to begin with and was not pinned to the template at any instance. Remarkably, CF contact angles on 80 and 90 wt % templates showed a rapid change during the first 500 μs of the measurement, decreasing by 40 and 30%, respectively. We ascribe this phenomenon to the enriching of IL at the ion gel surface upon contact with CF, which is further supported by MD simulations (discussed below). Although 50−90 wt % templates showed comparable surface composition under vacuum (Figure 2E), their interfacial properties differ upon exposure to CF because of higher reconfigurability of 80 and 90 wt % ion gels. We also measured receding contact angles of CF on various templates (Figure S6C,D), which fell within a narrow range of 6−11° and showed only slight template dependence; this implies that during MGC, the dependence of evaporation rate on the template is minor, as evidenced by similar film thicknesses measured (shown later).

To evaluate our hypothesis that IL enrichment at the ion gel surface underlies the rapid change in the contact angle upon exposure to CF, we investigated the ion gel interfacial properties via MD simulations with full atomic details. First, we validated the ion gel structure by calculating the bulk ionic conductivity from MD simulations and comparing it to the experimental values obtained from impedance spectroscopy (Figure S7A−C). Next, we characterized the ion gel interfacial structure upon exposure to vacuum versus CF. As shown in Figure S8A,B, the ion gel structure remains invariable after 240 ns of contact with vacuum. However, the IL concentration at the ion gel surface increases dramatically upon exposure to CF. We further quantified this observation by calculating [EMIM]-[TFSI] ion distribution orthogonal to the ion gel surface (along the z-coordinate of the simulation box), summarized in Figure S8C. These results clearly show that IL ions move to the ion gel surface to interact with CF, leading to >43% broadening of ion distribution along the z-coordinate. For more details on MD simulation studies, see the Supporting Information.

Template-Induced Multiscale Morphology of Conjugated Polymers. We next characterized thin-film morphology to understand how substrate dynamics and chemistry impact conjugated polymer crystallization and assembly. We quantified polymer chain alignment, molecular orientation ordering, and degree of crystallinity using a variety of techniques including cross-polarized optical microscopy (C-POM), atomic force microscopy (AFM), polarized ultraviolet−visible spectroscopy (UV−vis), and grazing incidence X-ray diffraction (GIXD).

First, we performed C-POM to qualitatively compare the effect of various substrates on DPP-BTz and PII-2T thin film in-plane alignment and global crystallinity as well as device

DOI: 10.1021/acsami.9b02923
ACS Appl. Mater. Interfaces 2019, 11, 22561−22574

scale morphology (Figures 3A and S9). The higher the normalized optical birefringence of the printed polymer film, the greater its degree of alignment and/or crystallinity (for more details, refer to our previous studies[15−17]). We quantified C-POM birefringence by calculating the average intensity difference of samples oriented 0° and 45° relative to the polarizer axis. The films coated on polymer-rich substrates were barely birefringent, and with the increase of template IL content, the birefringence was significantly increased. Surprisingly, DPP-BTz films coated on 80 and 90 wt % IL templates exhibit birefringence even higher than the 100 wt % neat IL (Figure 3D). We observed such consistent trend for PII-2T films with even more pronounced maximum birefringence at 80 and 90 wt % IL templates (Figure S9D). Elevating the coating temperature further enhances DPP-BTz thin film in-plane alignment (Figure S10).

Followed by C-POM measurements at the macroscale, we used AFM to characterize conjugated polymer film mesoscale morphology such as fibril/domain size and orientation. AFM height images for DPP-BTz (Figure 3B) and PII-2T films (Figure S9B) showed a significant increase in crystallite size compared to films coated on polymer-rich (∼10 nm) and IL-rich templates (∼1−10 μm). We measured the film thickness by AFM for both conjugated polymers (Figure S11), which was essentially invariant across the entire spectrum of template compositions. This observation is consistent with the receding contact angle measurements (Figure S6C,D). Similar film thickness allows us to directly compare film morphologies across the template composition range.

To quantify polymer chain alignment, we carried out polarized UV−vis spectroscopy and again observed a non-monotonic trend pointing to the synergy between the IL and the polymer matrix in enhancing the templating effect. Figure 3C summarizes normalized UV−vis absorption spectra for the templated DPP-BTz films, with the polarized light parallel and perpendicular to the coating direction. Higher absorbance in the perpendicular configuration informs that the polymer backbone is preferentially oriented perpendicular to the coating direction, given that the transition dipole usually has the largest component along the long axis of the polymer backbone.[12,44,45] The degree of in-plane alignment substantially enhanced with the increase of the IL content in the ion gel, quantified by the 0−0 vibronic peak dichroic ratio, $R_{UV-vis} = I_{per}/I_{par}$ (Figure 3D). For DPP-BTz, R_{UV-vis} was 1.9 ± 0.1 for the neat polymer matrix e-P(VDF:HFP) and had an increasing trend reaching the value of 6.6 ± 0.2 for 90 wt % IL templates. The IL-coated film had an R_{UV-vis} of 5.1 ± 0.6, which further confirms the synergistic templating effect of the IL and polymer matrix. It should be considered that R_{UV-vis} provides a lower bound to the degree of alignment depending on polymer chain curvature and its solid-state conformation.[44,45] PII-2T UV−vis characterizations (Figure S9C,D) essentially showed the same effect; the overall lower dichroic ratios were attributed to twinned crystalline domains reported previously as well.[15] Overall, the UV−vis dichroic ratio follows the same trend as that of CPOM birefringence, both showing pronounced and systematic modulation of conjugated polymer in-plane alignment by tuning template dynamics and composition and a surprising synergetic effect. Besides dichroic ratio, we observed a blue shift of the 0−0 peak position from 873 to 846 nm and a decreasing 0−0/0−1 peak ratio in the perpendicular spectra of DPP-BTz with increasing IL content of the template (Figure S12); both suggest enhanced H-aggregation resulted from stronger interchain $\pi-\pi$ interactions.[46] This observation is consistent with increased domain size from AFM measurements and higher degree of ordering inferred from the GIXD study discussed below.

We next used GIXD (Figure S13) to characterize molecular packing, relative degree of crystallinity (rDoC), in-plane alignment of crystalline domains, and out-of-plane crystallite orientation distribution. GIXD measurement unveiled a dramatic molecular orientation transition from predominantly "face-on" to mostly "edge-on" in DPP-BTz films with increasing IL content in the template (Figure 4A). Polymers coated on the polymer-rich substrates exhibited a well-defined face-on $\pi-\pi$ stacking diffraction (010) along with pronounced in-plane lamellar stacking peaks, visible up to (300), in both parallel and perpendicular directions. For IL-rich templates, the polymer backbone was preferentially oriented "edge-on" and perpendicular to the coating direction, and out-of-plane lamella peak was easily discernible up to (500). We observed the most intense edge-on $\pi-\pi$ stacking peak and correspondingly the weakest face-on peak intensity for the 80 wt % ion gel and not the neat IL. To quantitatively express the orientation distribution of crystalline domains, we extracted pole figures[47] using the procedure described in our previous reports.[11,17] In Figures 4B and S14A, (010) and (200) peak intensities are plotted as a function of the polar angle χ and the in-plane rotation angle of the substrate, φ, at IL contents of 0, 80, and 100 wt %. In these figures, the "face-on" crystallites are described by the (010) peak at $\chi = 90°$ and the (200) peak at $\chi = 0°$ and the "edge-on" crystallites by the (010) peak at $\chi = 0°$ and the (200) peak at $\chi = 90°$. The pole figures quantitatively validated the molecular orientation transition described above. Notably, the population of 80 wt % edge-on crystallites is significantly higher than 100 wt % neat IL-templated films. Figure S14B,C summarizes DPP-BTz stacking distances, full width at half-maximum (fwhm), and geometrically normalized peak area. The lamellar stacking distance increased by up to 3% comparing IL-rich templates with the neat polymer matrix. To verify the generality of this molecular orientation transition, we characterized PII-2T via GIXD (Figure S15A−C) and observed a similar phenomenon. The lamellar stacking distance in PII-2T films increased with increasing "edge-on" population as well. Such "face-on" to "edge-on" orientation transition accompanied by increased lamellar stacking distance suggests that IL-rich ion gel dynamic templates enhanced conjugated polymer self-interactions so as to expedite their crystallization; this is in contrast to strong conjugated polymer−substrate interactions in the case of polymer-rich templates of slower dynamics/higher T_g. Enhanced conjugated polymer self-interactions may have originated from highly enriched conjugated polymer concentration near effective dynamic templates shown in our previous work.[15]

We now turn our attention to in-plane alignment inferred from the pole figure. From Figure 4A,B, most conditions exhibit more intense edge-on $\pi-\pi$ stacking peak in the perpendicular scans ($\varphi = 90°$) than in the parallel scans ($\varphi = 0°$), verifying UV−vis data that the polymer backbone preferentially oriented perpendicular to the coating direction for edge-on crystallites. The normalized edge-on $\pi-\pi$ peak area comparing parallel scans with perpendicular scans indicated that the maximum in-plane anisotropy occurred at the 80 wt % IL content (Figure 4C). We quantified the in-plane alignment using the dichroic ratio defined as $R_{GIXD} = A_{\perp}/A_{\parallel}$, where $A_{\perp}$ and $A_{\parallel}$ are the normalized edge-on $\pi-\pi$

DOI: 10.1021/acsami.9b02923
ACS Appl. Mater. Interfaces 2019, 11, 22561−22574

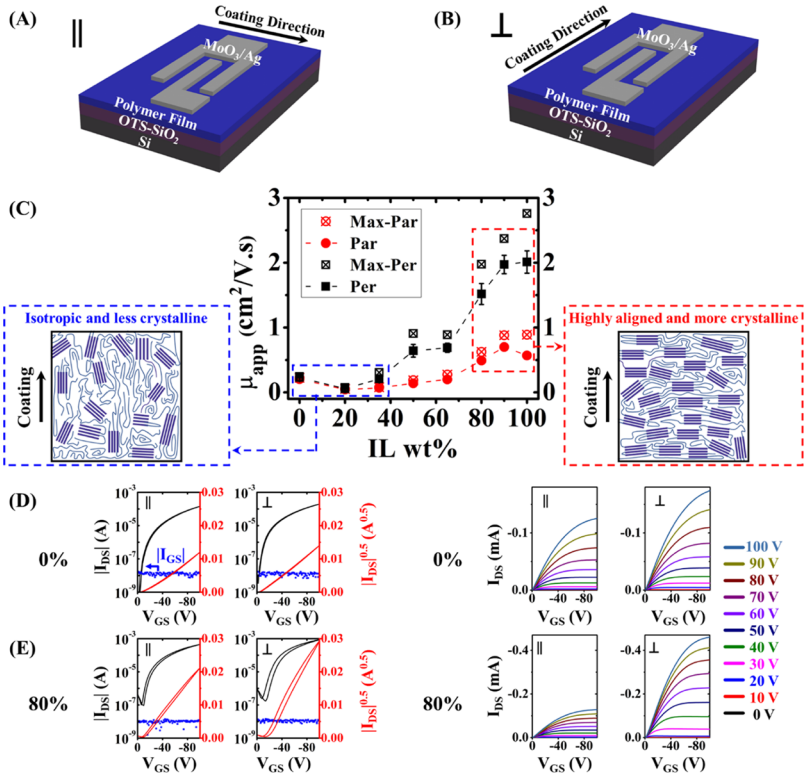

Figure 5. DPP-BTz morphology-dependent charge transport properties in FET devices. Schematic of (A) parallel and (B) perpendicular BGTC device configuration with 8 nm thick molybdenum oxide (MoO_3) and 35 nm thick silver (Ag) as source and drain electrodes, OTS-treated 300 nm thick SiO_2 dielectric layer, and doped silicon gate terminal. (C) Apparent hole mobility measured in parallel and perpendicular directions with respect to the coating direction as a function of template composition, extracted from the saturation regime at $V_{DS} = -100$ V. In the inset, in-plane mesoscale morphology is depicted, highlighting highly aligned and crystalline semiconducting polymer films coated on IL-rich ion gels, leading to high-performance OFETs. (C,D) Representative transfer and output curves corresponding to films coated on templates with (D) 0 and (E) 80% IL parallel and perpendicular to the coating direction. The gate current (I_{GS}) is plotted as blue scatters to assess the leakage current.

Table 1. Summary of the Key FET Parameters for DPP-BTz Devices

	parallel			Perpendicular		
substrate IL wt %	μ_{app} (max) (cm^2V^{-1} s^{-1})	log (I_{on}/I_{off})	V_{th} (V)	μ_{app} (max) (cm^2V^{-1} s^{-1})	log (I_{on}/I_{off})	V_{th} (V)
0	0.20 ± 0.01 (0.22)	5.4 ± 1.0	−10.7 ± 1.3	0.23 ± 0.01 (0.24)	5.4 ± 2.3	−6.5 ± 1.8
20	0.04 ± 0.01 (0.05)	5.0 ± 2.3	−19.7 ± 1.1	0.06 ± 0.01 (0.08)	4.8 ± 1.2	−18.7 ± 0.7
35	0.07 ± 0.01 (0.08)	5.0 ± 2.2	−16.3 ± 1.1	0.21 ± 0.03 (0.31)	5.8 ± 2.1	−14.0 ± 0.6
50	0.14 ± 0.02 (0.19)	5.2 ± 1.1	−16.2 ± 1.3	0.64 ± 0.10 (0.91)	5.5 ± 2.1	−16.7 ± 0.8
65	0.20 ± 0.02 (0.28)	6.2 ± 2.5	−13.2 ± 1.7	0.69 ± 0.07 (0.89)	5.5 ± 1.9	−15.0 ± 1.7
80	0.49 ± 0.05 (0.62)	6.7 ± 2.6	−16.3 ± 0.8	1.52 ± 0.01 (1.98)	3.7 ± 0.6	−13.2 ± 0.9
90	0.70 ± 0.06 (0.88)	5.5 ± 1.9	−13.0 ± 2.2	1.97 ± 0.14 (2.37)	4.0 ± 0.4	−16.2 ± 0.9
100	0.57 ± 0.07 (0.89)	4.0 ± 1.2	−8.2 ± 1.2	2.01 ± 0.18 (2.76)	3.6 ± 1.4	−11.8 ± 1.1

stacking peak area with the incidence beam perpendicular and parallel to the coating direction, respectively. The highest R_{GIXD}, corresponding to the film coated on the 80 wt % IL, exceeded 55 which is over 50 times higher than R_{GIXD} for the neat e-P(VDF:HFP) template (Figure 4D). This extraordinary enhancement in the in-plane alignment of crystalline domains is consistent with C-POM and UV−vis results. The significantly higher anisotropy from GIXD measurements suggests that the crystalline domains are driving the overall alignment of the polymer backbone. A similar trend was observed for PII-2T films (Figure S14D), albeit with lower degree of anisotropy because of twinned domains. Most interestingly, conjugated polymer films coated on neat IL had lower degree of alignment compared to 80 wt % and/or 90 wt % IL ion gels, which once again signifies the synergistic templating effect of the IL and the polymer matrix consistent with C-POM and UV−vis observations.

We further performed a quantitative analysis on the rDoC of the conjugated polymer thin films by integrating the normalized, geometrically corrected peak intensities over χ and φ (Figure 4E). We found that the rDoC of thin films templated by the 80 wt % IL template was ∼50% higher compared to the neat polymer template and was even 26% higher than the neat IL case. It is worth mentioning that such a drastic improvement in the polymer degree of alignment and crystallinity is not achievable simply by varying the coating conditions or the choice of solvent. Such enhanced rDoC is consistent with our hypothesis that IL-rich ion gel dynamic templates enhanced conjugated polymer crystallization through promoting polymer self-interactions.

DOI: 10.1021/acsami.9b02923
ACS Appl. Mater. Interfaces 2019, 11, 22561−22574

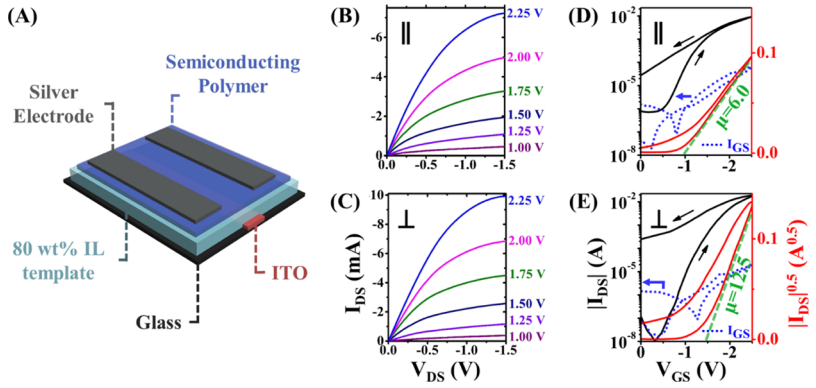

Figure 6. High-performance OECT devices using an ion gel as both the dynamic template and the gate dielectric layer. (A) Schematic of the BGTC device configuration with silver (Ag) as the source and drain electrode, 80 wt % IL ion gel as the dielectric layer, and indium−tin−oxide (ITO)-patterned glass as the gate terminal. Representative (B,C) output and (D,E) transfer curves of corresponding devices with the channel length parallel (B,D) and perpendicular (C,E) to the coating direction. A saturation current more than 9 mA is obtained at V_{GS} = −2.5 V and V_{DS} = −1.5 V as a result of dynamic-template-enhanced film morphology and high capacitance of the ion gel. Hysteresis is evident between the forward and reverse traces consistent with previous reports implementing ion gels as the dielectric layer. Apparent hole mobility (extracted from the saturation regime) as high as 12.5 (6.0) $cm^2\ V^{-1}\ s^{-1}$ was measured perpendicular (parallel) to the coating direction. The average on/off ratios for the devices parallel and perpendicular to the coating direction are $(3.0 \pm 2.0) \times 10^4$ and $(7.5 \pm 2.0) \times 10^5$. The average threshold voltages for parallel and perpendicular devices are −0.72 ± 0.14 and −0.88 ± 0.11 V, respectively.

Morphology-Dependent FET Performance. To establish the morphology−charge transport property relationship, we measured charge carrier mobilities by fabricating FETs. Overall device performance was significantly improved for devices coated on IL-rich dynamic templates as a result of enhanced alignment and rDoC. To quantify the preferred charge transport pathway and anisotropy, we fabricated bottom-gate, top-contact (BGTC) FETs with the channel length parallel and perpendicular to the coating direction (Figure 5A,B). The as-coated polymer films were transferred to ODTS-treated SiO_2/Si substrates to allow direct comparison among different film morphologies (see the Experimental Section for fabrication details). The apparent hole mobilities (μ_{app}) were extracted from the transfer curves measured in the saturation regime and summarized in Figure 5C. The characteristic transfer and output curves comparing the devices coated on templates of 0 and 80 wt % IL are shown in Figure 5D,E (all transfer and output curves are summarized in Figure S16). Table 1 summarizes the key FET parameters. Most transfer curves are free from "kinks" commonly observed in high-performance devices. The average reliability factor in FETs was calculated to exceed 50%.[48]

Figure 5C presents a systematic enhancement of μ_{app} with increasing IL content in the dynamic templates, with the average μ_{app} increased from 0.2 ± 0.1 to 0.7 ± 0.1 $cm^2\ V^{-1}\ s^{-1}$ parallel (along π−π stacking) and from 0.2 ± 0.1 to 2.0 ± 0.2 $cm^2\ V^{-1}\ s^{-1}$ perpendicular (along conjugated backbone) to the coating direction, compared to neat-polymer-templated devices. We attribute such significant enhancement in hole mobilities to boosted in-plane alignment and increased degree of crystallinity in films coated on IL-rich templates. Interestingly, best performing devices were fabricated from IL-templated films with μ_{app} exceeding 2.8 and 0.9 $cm^2\ V^{-1}\ s^{-1}$ along the backbone and π-stacking directions, despite higher in-plane alignment and crystallinity in 80 wt % ion-gel-templated films. This could be associated with bimodal "face-on" and "edge-on" crystallite orientation distribution in IL-templated films, compared to dominantly "edge-on" orientation in 80 wt % ion-gel-templated films. It was shown in some cases that bimodal orientation yielded superior mobility possibly because of the formation of three-dimensional conduction pathways.[49−51]

Furthermore, we observed favorable charge transport along the polymer backbone in highly aligned films. Charge transport anisotropy ($R_{FET} = \mu_{per}/\mu_{par}$) strongly depends on polymer chain alignment, and while R_{FET} is more than 3 for IL-templated films, it is almost unity for the neat polymer matrix-templated films. The extent of charge transport anisotropy is substantially lower than in-plane alignment quantified by UV−vis and X-ray.[12,14,15,52] This is not surprising because charge transport is limited by grain boundaries, chain ends, and at times amorphous domains, which were not accounted for in ensemble-averaged degree of alignment and crystallinity.

We also tested charge transport properties of PII-2T films templated by the ion gel series (Figure S17). With increasing IL content in the ion gel, μ_{app} remained similar in the parallel direction (along π−π stacking) within the range of error but increased to peak at the 80 wt % IL content in the perpendicular direction (along the conjugated backbone) to a value more than 4 times than that at 0 wt % IL. Larger crystallite size, higher degree of alignment, and crystallinity in IL-rich ion-gel-templated PII-2T films significantly improved charge transport along the polymer backbone. However, twin boundaries perpendicular to coating (Figure S9) may be the limiting factor hindering charge transport along the π−π stacking direction. Figure S18 summarizes transfer, output, and gate voltage-dependent saturation hole mobility for best performing devices at each condition. Again, most transfer curves were free of kinks with calculated reliability factor more than 50% for the whole series. We note that no exhaustive effort was spent on optimizing the device performance as the primary focus is on morphology−device property relationship in this study. Table S2 summarizes the key FET parameters.

Demonstrating Dual Functionality of Ion Gels as Dynamic Templates and Gate Dielectrics. It is well-demonstrated that ion gels are great candidates for gate dielectrics in printed electronics, given their solution processability, high capacitance, fast polarization response, and optical transparency.[53−55] The high capacitance of ion gel dielectrics is attributed to the formation of electrical double

DOI: 10.1021/acsami.9b02923
ACS Appl. Mater. Interfaces 2019, 11, 22561−22574

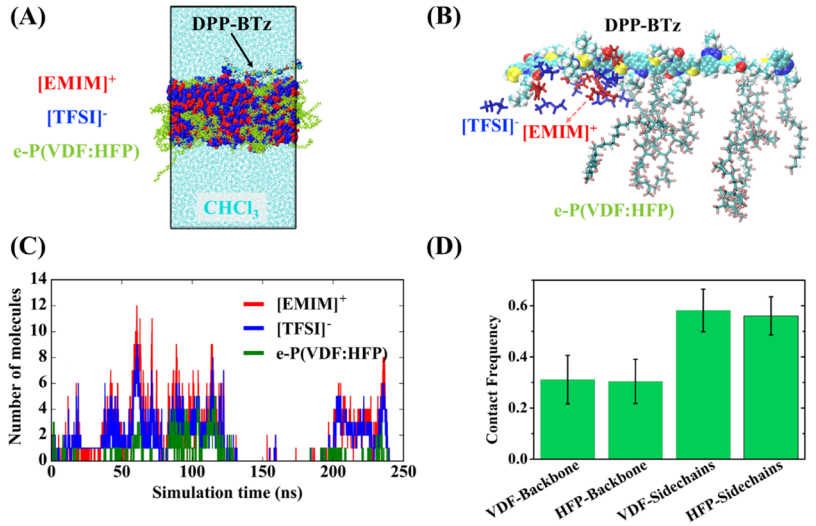

Figure 7. MD simulations investigating the interactions between the ion gel and DPP-BTz. (A) Representative snapshot illustrating the interaction between the ion gel template and DPP-BTz oligomer. (B) Snapshot of the simulated system illustrating the synergistic interaction between [EMIM][TFSI] and e-P(VDF:HFP) with the DPP-BTz oligomer. The black line indicates the periodic simulation box. (C) Number of $[EMIM]^+$ and $[TFSI]^-$ ions and e-P(VDF:HFP) chains within a distance of 5 Å from the DPP-BTz tetramer as a function of simulation time. Decoupling the contribution of the IL and polymer matrix in the overall interaction implies that IL and e-P(VDF:HFP) simultaneously interact with DPP-BTz at the ion gel interface. (D) Contact frequency of the conjugated backbone and the side chains of DPP-BTz with VDF and HFP blocks of e-P(VDF:HFP). The contact frequency is calculated by counting the total number of frames that have molecular contact between the individual parts of DPP-BTz and e-P(VDF:HFP), normalized by the total number of frames that have contact between DPP-BTz and e-P(VDF:HFP). A contact is counted if the minimum distances between the partial structures of DPP-BTz and e-P(VDF:HFP) are less than 5 Å. The error bars on the contact frequency were determined by dividing the simulation trajectories into three blocks and calculating the standard deviation of the block average contact frequencies.

layers (EDLs), which enables high-performing transparent transistors operated at low voltage. Above, we demonstrated comprehensively the use of ion gels as dynamic templates for enhanced morphology and electrical properties of conjugated polymer thin films. Next, we combine these advantages with the exceptionally high capacitance of ion gels for the fabrication of high-performance ion-gel-gated organic electrochemical transistor (OECT) devices. We used 80 wt % IL ion gels to prepare BGTC devices with DPP-BTz as the semiconducting layer. Device configuration is depicted in Figure 6A, and the corresponding optical microscopy image is shown in Figure S19A (see the Experimental Section for fabrication details). Typical output and transfer characteristics are shown in Figure 6D,E, measured with the channel length parallel (along $\pi-\pi$ stacking) and perpendicular (along conjugated backbone) to the coating direction. Output curves exhibited excellent gate modulation of the drain current, and at high V_{DS}, I_{DS} clearly becomes saturated. The saturation current is close to 10 mA at low $V_{GS} = -2.25$ V and $V_{DS} = -1.5$ V, a direct result of high charge carrier mobility in exceptionally ordered DPP-BTz and the high capacitance of ion gels. Transfer characteristics show linear dependence of $|I_{SD}|^{1/2}$ as a function of V_{GS} in the saturation regime, with low gate leakage current which is approximately 3 orders of magnitude lower than the drain current at $V_{GS} > V_{th}$ (Figure S19B,C). On the basis of previous works, ion gel capacitance measured by impedance spectroscopy strongly depends on frequency.[53,55,56] To accurately calculate charge carrier mobility, we measured the specific capacitance of the employed dielectric layer using quasi-static capacitance measurements as a frequency-independent method (Figure S20). We calculated the capacitance of a 2 μm thick 4:1 wt ratio [EMIM][TFSI]:e-P(VDF:HFP) dielectric layer to be 29 ± 2 $\mu F/cm^2$ from more than 10 independent devices, which is in good agreement with frequency-dependent measurements reported previously for [EMIM][TFSI]-based ion gel dielectrics, extrapolated to the zero-frequency limit.[54−57] We note that the capacitance at the zero-frequency limit is most relevant to our case. Correspondingly, the apparent hole mobilities in the saturation regime averaged 3.5 ± 1.0 and 7.2 ± 1.3 $cm^2\ V^{-1}\ s^{-1}$ in the parallel and perpendicular directions, respectively (Figure S19D−G). The μ_{app} is calculated rigorously by averaging the hole mobility over the entire hysteresis loop to avoid overestimations.[48] It should be noted that the gate current leakage is rather large (Figure 6D,E) and off-current increases after continuous measurements (Figure S19F). These phenomena are attributed to ion gel high ionic conductance and ion movement toward the semiconductor layer upon consecutive measurements.[58−60] For parallel and perpendicular devices, the I_{DS} to I_{GS} ratios are (6.6 ± 1.3) × 10^2 and (3.0 ± 0.3) × 10^3, respectively, within the range that μ_{app} is extracted.

DISCUSSION

As discussed above extensively, our multiscale morphology characterizations revealed a synergistic effect between the IL and the polymer matrix in IL-rich ion gels. As a result, conjugated polymer alignment and crystallinity were improved significantly beyond the levels achieved using either the neat IL or the neat polymer templates. Compared to 100 wt % IL-templated thin films, the in-plane alignment for DPP-BTz films deposited on 80−90 wt % IL templates is ∼28% higher determined by C-POM birefringence and polarized UV−vis, the "edge-on" $\pi-\pi$ stacking peak is twice as intense, and the rDoC exhibited a ∼27% increase from GIXD analysis. We hypothesize that this phenomenon is attributed to synergistic multivalent interactions of the two components of the ion gel

DOI: 10.1021/acsami.9b02923
ACS Appl. Mater. Interfaces 2019, 11, 22561−22574

with the conjugated polymer, facilitated by rapid adaptability of the ion gel template evident from contact angle measurements and MD simulations. We believe that the synergy in the multivalent interactions arises from complementary chemistries of IL and e-PVDF-HFP, which associate with different "binding sites" of the conjugated polymer. Such cooperative multivalent interactions have been studied extensively in other areas.[61−63]

To test this hypothesis and to gain further insights on the intermolecular interactions, we carried out MD simulations on the CF solution of the DPP-BTz oligomer in contact with the ion gel template (Figures 7A and S21A). Consistent with our previous work,[15] the conjugated oligomer formed a concentrated layer near the ion gel surface with >8 times the distribution probability relative to the bulk solution (Figure S21B). This is a result of strong interaction between DPP-BTz and the ion gel template. We next turned our attention to the role of ion gel components in the binding process. Simulation snapshots (e.g., Figure 7B) clearly show that both [EMIM][TFSI] and e-P(VDF:HFP) interact with the conjugated molecule. This is quantified in Figure 7C by calculating the number of species in contact with DPP-BTz at each time. As expected, the IL (esp. the cation) interacts significantly stronger than the polymer matrix. However, most importantly, this result shows that the IL ions and the polymer matrix interact simultaneously with the conjugated molecule, signifying the synergistic enhancement in the overall interaction.

In addition, from simulation snapshots, we noticed that e-P(VDF:HFP) does not line up with the oligomer backbone and mainly interacts with the alkyl side chains. We evaluated this observation by calculating the contact frequency between the polymer matrix blocks and the conjugated molecule (Figure 7d). Notably, e-P(VDF:HFP) interacts with alkyl side chains almost two times stronger than with the conjugated backbone. This is opposite to the IL, which mainly interacts with the conjugated core demonstrated by ^{1}H NMR measurements.[15] In conclusion, the complementary chemistries of IL and e-P(VDF:HFP) in the ion gel enable multivalent binding with the conjugated polymer. Specifically, the IL interacts with the conjugated backbone via electrostatic and ion−π interactions and e-P(VDF:HFP) interacts with the alkyl side chain via van der Waals interactions. The outcome of such complementary multivalent binding is a synergistic templating effect induced by the ion gel that outperforms both neat phases.

CONCLUSIONS

In summary, we designed ion gel dynamic templates of widely tunable dynamics with T_g spanning from −20 to −93 °C by varying the ion gel composition. Although surface-sensitive XPS characterizations showed that the IL content on the ion gel surface did not exceed ∼55 wt % in vacuum, dynamic contact angle measurements demonstrated that the ion gel surface composition can adapt within <500 μs in response to the ink environment. These results were further verified by MD simulations, showing 43% increase in surface IL content upon exposure to the solvent. Next, we systematically modulated conjugated polymer thin-film morphology during solution coating by tuning the ion gel template composition and therefore dynamics. Our comprehensive multiscale morphology characterizations of ion-gel-templated DPP-BTz thin films showed that as the IL content of the ion gel increases from 0 to 80−90 wt %, the film exhibited 4.6 times higher birefringence and 3.5 times higher and 50 times higher UV−vis and GIXD dichroic ratios, respectively, indicating improved in-plane alignment. At the same time, the rDoC increased by almost 50%. Moreover, the out-of-plane molecular orientation transitioned from "face-on" to "edge-on". We infer that such drastic morphology change is due to enhanced conjugated polymer self-interactions and expedited crystallization as the ion gel dynamics increases. The compound effect of higher degree of alignment and crystallinity for films coated on IL-rich ion gels led to significantly improved apparent hole mobility along both the polymer backbone (from 0.3 to 2.8 cm^2 V^{-1} s^{-1}) and the π-stacking direction (from 0.3 to 1.1 cm^2 V^{-1} s^{-1}), compared to devices templated by the neat polymer matrix. Finally, we also employed the ion gel template as a high-capacitance dielectric layer to attain TFTs with average apparent hole mobility as high as 11.8 cm^2 V^{-1} s^{-1} along the conjugated backbone. Throughout the study, we used a second conjugated polymer PII-2T to ensure the generality of the dynamic templating effect. For both polymer systems, we observed a surprising synergistic effect that there exists an optimal IL to polymer matrix ratio of the ion gel, which outperformed both the neat IL- and the neat polymer matrix-based templates. Through MD simulations, we elucidated that such synergy between the IL and the polymer matrix could arise from their cooperative multivalent binding with the conjugated polymers. We anticipate that our novel dynamic templating method and mechanistic insights will help enable exquisite morphology control for high-performance printed electronics and other functional soft matter.

EXPERIMENTAL SECTION

Dynamic Template Preparation and Characterizations. We prepared ion gel dynamic templates by codissolving the IL, [EMIM][TFSI] (≥98%; purchased from Solvionic), and e-P(VDF:HFP) with the VDF to HFP molar ratio of 55:45 (Dyneon Fluoroelastomer FE purchased from 3M Company) in room-temperature acetone (Optima grade, Fisher Scientific) stirring for >3 h to fully dissolve. The weight ratio between e-P(VDF:HFP) and acetone was kept at 1:8, and [EMIM][TFSI] weight was adjusted accordingly based on the desired mixing ratio. The clear and homogeneous solution was spin-coated on Corning glass substrates at 2000 rpm for 1 min using on-the-fly-dispensing method.[64] The substrates were then left to dry overnight at 80 °C in an inert environment (nitrogen glovebox). All obtained films were transparent, and their thickness was 1−2 μm (estimated by tapping-mode AFM measurements and optical microscopy). Thus, we believe none of the microstructural and morphological transitions would depend on the template film thickness. Substrates with neat IL defining the surface chemistry were prepared with the same procedure reported in our previous work.[15]

Thermal transition measurements were conducted using Q20 (TA Instruments) differential scanning calorimeter from −90 to 15 °C at cooling/heating rates of 10 °C·min^{-1} with argon as the carrier gas. Samples weighing ∼4−8 mg were prepared by drop-casting the solution on a glass substrate, annealing to remove the solvent for >24 h, and transferring the films to a sealed hermetic aluminum pan for measurements by pealing them off. FTIR spectroscopy was conducted using a Nicolet iS5 FTIR spectrometer at ambient temperature on elastomer-IL hybrid films, spin-cast on silicon substrates with different weight ratios in the range of 500−4000 cm^{-1} with a wavenumber resolution of 1 cm^{-1} (step size of <0.5 cm^{-1}). XPS data were obtained via a Kratos Axis Ultra XPS system (Krato Analytical Ltd.) under high vacuum (1 × 10^{-9} Torr) with a monochromatic Al Kα X-ray source (14 kV, 10 mA). Incidence angle was set at 90°, resulting in penetration depth <10 nm. High-resolution XPS spectra were

DOI: 10.1021/acsami.9b02923
ACS Appl. Mater. Interfaces 2019, 11, 22561−22574

obtained at a constant pass energy of 40 eV, a step size of 0.1 eV, and an exposure time of 400 ms. Peak analysis and deconvolution were performed with CasaXPS software. For sessile contact angle measurements, the known volume of the CF sessile droplet was gently placed on the substrate, and evaporation was monitored in an experimental cell avoiding external air flow perturbations. The droplet evaporation was recorded using a digital camera, and after image processing geometrical parameters were estimated as a function of time using drop shape analyzer software (DROPimage Ramé-hart). Receding contact angle measurements were carried out using a microsyringe with a stainless steel flat needle, and quasi-static contact receding contact angle was measured while the droplet volume was shrinking.

Conjugated Polymer Thin-Film Fabrication. Poly[[2,5-bis(2-octadecyl)-2,3,5,6-tetrahydro-3,6-diketopyrrolo[3,4-*c*]pyrrole-1,4-diyl]-*alt*-(2-octylnonyl)-2,1,3-benzotriazole] (DPP-BTz) (M_n = 176 kg·mol^{-1} and PDI = 2.5) and PII-2T (M_n = 118 kg·mol^{-1} and PDI = 2.5) were synthesized as reported before.[12,15,17,18] DPP-BTz (PII-2T) solution was prepared by dissolving the polymer semiconductor in anhydrous CF (Macron ACS grade) at 5.0 (7.5) mg/mL and stirred until a clear homogeneous solution was obtained. Semiconducting polymer thin films were deposited onto substrates by a MGC method using an ODTS-treated Si blade.[15] The MGC setup involves a stationary substrate and a moving blade, with ink solution sandwiched in between. The blade was tilted by 8°, with the blade edge set 100 μm above the substrate surface for the film deposition process. The substrate temperature was fixed at 25 °C, and the speeds of the blade were 0.25 and 0.5 mm/s for depositing DPP-BTz and PII-2T, respectively.

For C-POM, AFM, and GIXD measurements, the as-coated polymer films were transferred to the ODTS-functionalized silicon wafer with 300 nm thermally grown SiO_2 by the following procedure. First, the ODTS-treated substrate was brought in contact with the as-coated film by placing it inversely atop. After establishing the interface contact, the whole sandwiched structure was immersed in an orthogonal solvent (acetonitrile) that is capable of dissolving an ion gel template but keeping the conjugated polymer film intact. Meanwhile, an external force was imposed on the ODTS substrate fixing the sandwiched structure. After 12 h, the film was completely transferred, and the ODTS substrate with a conjugated polymer film atop was immersed in a fresh acetonitrile bath for another 12 h to remove remaining residuals. Finally, the ODTS substrate with the transferred film atop was dried with nitrogen gas and stored in an inert glovebox overnight to remove the remaining acetonitrile. This generic transfer method allows for direct comparison across the series of substrates and avoids the active layer of the semiconductor being doped by the template.

Thin-Film Morphology Characterizations. We visualized polymer films using a Nikon Ci-POL optical microscope to observe birefringence under crossed polarized light. To quantify birefringence as a function of template IL content, we measured the average intensity of several random cross sections within each image to calculate its brightness. Then, we calculated the intensity difference of the film when coating direction was oriented 0° versus 45° with respect to the polarizer axis. Larger values correspond to higher birefringence of the polymer film. The sample was centered on a microscope stage so that the obtained images correspond to the same area, while the stage was rotated. Tapping-mode AFM measurements were carried out using an Asylum Research Cypher instrument (Asylum Research) to compare the mesoscale morphologies and measure the semiconducting layer thickness. Solid-state transmission UV−vis spectroscopy measurements were recorded at room temperature on an Agilent Cary 60 UV−vis spectrometer, with the incident light polarized vertically via a broadband sheet polarizer. The as-coated films on various templates were scanned within the wavelength of 400−1000 nm after subtracting background. Samples were rotated relative to the coating direction to determine polymer chains. GIXD was performed at the small-/wide-angle X-ray scattering beamline 8-ID-E at the Advanced Photon Source (Argonne National Laboratory) with an X-ray wavelength of 1.14 Å (E_{beam} = 10.92 keV), with a two-dimensional Pilatus 1M detector for data collection.[65] For GIXD measurements, all semiconducting polymer films were transferred to ODTS-treated Si substrates with native oxide (keeping all substrate's background diffractions invariant) and scanned in a helium chamber, with a 278 mm sample-to-detector distance. The incidence angle was 0.14°, and the exposure time was 10 s. Each sample was scanned at various in-plane rotation angles, φ, by rotating the substrate with respect to the incidence beam (Figure 4) by 0°, 30°, 60°, and 90°. φ is defined as 0° (90°) when the coating direction is oriented parallel (perpendicular) to the incident beam. Data analysis was performed with the software GIXSGUI, which includes correction for the polarization of the synchrotron X-ray beam, detector nonuniformity, and sensitivity.[65,66] Partial pole figures were constructed by extracting $\pi-\pi$ stacking peak (010) intensities as a function of the polar angle, χ (binned into 9 sectors from 10 to 88°) to analyze out-of-plane crystallite orientation distribution as well as rDoC. To calculate the peak intensities, precise manual multipeak fitting was performed using Igor Pro software (WaveMetrics) on the intensity versus q curve obtained from each segment along the χ axis to deconvolute the $\pi-\pi$ stacking peak from the amorphous ring, SiO_2 scattering, and the ODTS peak. The peak intensity was automatically normalized because the irradiated volume remained the same across the samples by keeping the film area and thickness constant throughout substrate series (sample dimension was larger than the beam footprint). The edge-on $\pi-\pi$ stacking peak and the in-plane lamella stacking peak were obtained from a sector cut between $-88° < \chi < -83°$. Face-on $\pi-\pi$ stacking peak and the out-of-plane lamella stacking peak were obtained from a sector cut between $-15° < \chi < -10°$. The $\pi-\pi$ stacking peak was fitted with a Lorentzian function to obtain the diffraction parameters including peak position and area and fwhm.

Device Fabrication and Electrical Characterization. After transferring the semiconducting DPP-BTz and PII-2T films to highly n-doped Si (gate) with an ODTS-functionalized 300 nm SiO_2 layer (dielectric), BGTC FET configuration was fabricated by thermally evaporating 8 nm molybdenum oxide (MoO_3) and 35 nm silver (Ag) electrodes (source and drain) onto the polymer films via a shadow mask. XPS measurements showed no detectable IL residual within the top 10 nm of the polymer surface[15] where charge transport in FETs occurs. The channel length (L) was 47 μm, and the channel width (W) was 840 μm. All electrical measurements were performed in a nitrogen environment using a Keysight B1500A semiconductor parameter analyzer. The apparent hole mobilities were calculated from the saturation region (V_{DS} = −100 V) of transfer curves by the equation

$$I_{DS} = \frac{WC\mu_{app}}{2L}(V_G - V_{th})^2$$

where I_{DS} is the drain−source current, C_i is the capacitance of the dielectric (11 nF/cm^2 for the ODTS-treated 300 nm SiO_2 dielectric), V_{GS} is the gate voltage, μ_{app} is the apparent mobility, and V_{th} is the threshold voltage. W and L are the channel width and length of the transistors. Transfer characteristics were measured by sweeping from 0 to −100 V and back at the rate of 40 mV·s^{-1}. The average data were calculated from the analysis of more than 10 independent devices.

To fabricate OECTs with ion gels as the dielectric layer, polymer:IL solution was spin-coated, with the same condition described above, on patterned ITO/glass substrates. Next, the substrate was heated at 80 °C in a nitrogen glovebox overnight to physically cross-link the gel template. A 10 mg/mL DPP-BTz solution was coated atop serving as the semiconducting layer. Silver electrodes with an 80 nm thickness were thermally evaporated on the semiconducting layer via a shadow mask with a channel width and a length of 3750 and 45 μm, respectively. We only used silver as the source/drain electrode to minimize the electrode deposition time in a thermal evaporator and to avoid any damage to the soft ion gel dielectric/conjugated polymer interface that can lead to inferior TFT performance. Relatively large thickness of electrodes was used to ensure electrode connectivity, despite polymer film cracks ascribed to DPP-BTz high degree of crystallinity. The deposition rate was

DOI: 10.1021/acsami.9b02923
ACS Appl. Mater. Interfaces 2019, 11, 22561−22574

increased to 2 nm·s^{-1} for the same reason. The same instrumentation and measurement environment were used as explained above. However, source and drain terminals were connected using gold microwires in order to avoid short circuit by breaking into the semiconducting layer. The drain current was measured while sweeping V_{GS} from 0 to −1.5 V at a constant V_{DS} = − 1.5 V. The hole mobility of the transistors was calculated in the saturation regime similar to devices with the ODTS/SiO_2 dielectric layer. The device showed a reasonable ON/OFF current ratio of ∼10^4 to 10^5.

Quasi-Static Capacitance−Voltage Measurements. Quasi-static capacitance−voltage (QSCV) measurements were conducted using a conductor/dielectric layer/conductor structure wherein poly(3,4-ethylenedioxythiophene):poly(styrene sulfonate) (PEDOT:PSS) and Ag were used as the top and bottom electrodes, respectively, and ion gel template with 4:1 [EMIM][TFSI]:e-P(VDF:HFP) served as the dielectric layer. Silver electrodes were thermally deposited on glass substrates, and after IL:polymer solution was spin-coated on the substrate, 3.0−4.0 wt % high-conductivity grade PEDOT:PSS (Sigma-Aldrich) water solution was drop-cast on the ion gel, forming the top conductive layer. Overlapping area was measured by optical microscopy and later used for capacitance measurements. Upon sweeping the bias applied to the top contact from negative to positive voltage, capacitance was increased and then decreased in an almost symmetric manner to positive and negative carrier accumulations, respectively. A Keysight B1500A semiconductor parameter analyzer automatically measured the leakage current (I_{leak}) before and after the QSCV measurements and subtracted it out before reporting the final value. The capacitance was measured at $\Delta V/\Delta t$ = 0.1 and 0.2 V s^{-1} with voltage ranging from −3 to 3, −2 to 2, and −1 to 1 V, and results were independent of scan rate or voltage range. The quasi-static C is calculated from the measured current divided by the constant voltage change and area, $C = \frac{I\Delta t}{A\Delta V}$. We note that ion gel dielectric capacitance is thickness-independent because of EDL formation.

MD Simulations. All the MD simulations were set up using the AMBERTools14 and performed with full atomic details using the AMBER18 software package[67] and the general AMBER force field.[68] For all simulations, we began with an initial random configuration generated by the Packmol package[69] and then subjected the system to a long equilibration prior to the data collection and analysis. The e-P(VDF:HFP) polymer matrix was modeled as a triblock copolymer chain with 30 VDF units and 30 HFP units ($(VDF)_{15}(HFP)_{30}(VDF)_{15}$). The simulated DPP-BTz oligomer included 4 monomer units with their alkyl chains shortened to 1/3 of the original lengths given the constraints on the simulation box size. The starting structures of the individual molecules were drawn using the Maestro[70] and optimized by its built-in function. The modeled 80 wt % ion gel surface structure was validated by comparing the calculated ionic conductivities of the modeled ion gel and the neat ILs with the experimental data obtained from electrochemical impedance spectroscopy. All the simulations were performed with periodic boundary conditions in three dimensions using an integration step of 2 fs. For the simulation on the ion gel under vacuum, the system was maintained in constant-temperature and constant-volume (*NVT*) ensemble. For the simulations on DPP-BTz/CF and the ion gel templating substrate, each system was maintained in constant-temperature and constant-pressure (*NPT*) ensemble. For more details, see the Supporting Information.

■ ASSOCIATED CONTENT

Supporting Information

The Supporting Information is available free of charge on the ACS Publications website at DOI: 10.1021/acsami.9b02923.

MD simulations and analysis; ATR−FTIR and XPS composition-dependent peak analysis; contact angle measurements; EIS measurements for initial ion gel structure validation in MD simulation; C-POM, AFM, and UV−vis data and analysis for the PII-2T system; thickness measurements by AFM; UV−vis peak analysis; GIXD measurements setup, GIXD orientation and peak analysis; OFET characteristics and key parameters; OECT device characteristics; and QSCV capacitance measurements (PDF)

■ AUTHOR INFORMATION

Corresponding Author

*E-mail: yingdiao@illinois.edu.

ORCID

Chuankai Zhao: 0000-0002-6879-6514
Christopher M. Evans: 0000-0003-0668-2500
Jin-Kyun Lee: 0000-0001-9468-5749
Diwakar Shukla: 0000-0003-4079-5381
Ying Diao: 0000-0002-8984-0051

Present Address

[‖]School of Chemistry, University of Chinese Academy of Sciences, Beijing, 100049, P. R. China.

Author Contributions

E.M. and Y.D. designed the research project and Y.D. supervised the project. E.M. carried out the experiments and analyzed all the corresponding data. C.Z. and D.S. performed the MD simulations and analyzed the data. G.Q. and F.Z. performed the GIXD measurements and E.M. analyzed the data. F.Z. also helped partially with device fabrication and electrical characterizations. Q.Z. and C.M.E. helped with the electrochemical impedance spectroscopy measurements and E.M. analyzed the data. DPP-BTz semiconducting polymer synthesis was done by J.-K.L. and S.-H.J. (PII-2T). All authors discussed, revised, and approved the manuscript.

Funding

This project was funded primarily by NSF DMR Award #18-47828. E.M. acknowledges partial support by the NSF MRSEC: Illinois Materials Research Center under grant number DMR 17-20633. Y.D. acknowledges partial support from the Jiangsu Industrial Technology Research Institute (JITRI) through the JITRI International Fellowship Program. D.S. and C.Z. acknowledge the support from the Blue Waters sustained-petascale computing project, which is funded by the National Science Foundation (awards OCI-0725070 and ACI-1238993) and the State of Illinois.

Notes

The authors declare no competing financial interest.

■ ACKNOWLEDGMENTS

Portions of this research were carried out at the Advanced Photon Source, U.S. Department of Energy (DOE) Office of Science User Facility operated for the DOE Office of Science by Argonne National Laboratory under Contract No. DE-AC02-06CH11357. We appreciate help from beamline scientist Strazalka Joseph W. of Advanced Photon Source, Argonne National Laboratory facilitating the GIXD measurements. We also thank Professor Chao Wang from the Chemistry Department at the University of California at Riverside for kindly providing the elastomer e(PVDF:HFP). We would like to thank professor Jianguo Mei and graduate student Xuyi Luo for kindly providing the PII-2T conjugated polymer. This work was conducted in part in the Frederick Seitz Materials Research Laboratory Central Facilities, University of Illinois.

DOI: 10.1021/acsami.9b02923
ACS Appl. Mater. Interfaces 2019, 11, 22561−22574

REFERENCES

(1) Sirringhaus, H. 25th Anniversary Article: Organic Field-Effect Transistors: The Path Beyond Amorphous Silicon. *Adv. Mater.* **2014**, *26*, 1319−1335.

(2) Someya, T.; Bao, Z.; Malliaras, G. G. The rise of plastic bioelectronics. *Nature* **2016**, *540*, 379.

(3) Noriega, R.; Rivnay, J.; Vandewal, K.; Koch, F. P. V.; Stingelin, N.; Smith, P.; Toney, M. F.; Salleo, A. A general relationship between disorder, aggregation and charge transport in conjugated polymers. *Nat. Mater.* **2013**, *12*, 1038.

(4) Himmelberger, S.; Salleo, A. Engineering semiconducting polymers for efficient charge transport. *MRS Commun.* **2015**, *5*, 383−395.

(5) Venkateshvaran, D.; Nikolka, M.; Sadhanala, A.; Lemaur, V.; Zelazny, M.; Kepa, M.; Hurhangee, M.; Kronemeijer, A. J.; Pecunia, V.; Nasrallah, I.; Romanov, I.; Broch, K.; McCulloch, I.; Emin, D.; Olivier, Y.; Cornil, J.; Beljonne, D.; Sirringhaus, H. Approaching disorder-free transport in high-mobility conjugated polymers. *Nature* **2014**, *515*, 384.

(6) Dong, H.; Hu, W. Multilevel Investigation of Charge Transport in Conjugated Polymers. *Acc. Chem. Res.* **2016**, *49*, 2435−2443.

(7) Patel, B. B.; Diao, Y. Multiscale assembly of solution-processed organic electronics: the critical roles of confinement, fluid flow, and interfaces. *Nanotechnology* **2018**, *29*, 044004.

(8) Schuettfort, T.; Watts, B.; Thomsen, L.; Lee, M.; Sirringhaus, H.; McNeill, C. R. Microstructure of Polycrystalline Pbttt Films: Domain Mapping and Structure Formation. *ACS Nano* **2012**, *6*, 1849.

(9) DeLongchamp, D. M.; Kline, R. J.; Jung, Y.; Germack, D. S.; Lin, E. K.; Moad, A. J.; Richter, L. J.; Toney, M. F.; Heeney, M.; McCulloch, I. Controlling the Orientation of Terraced Nanoscale "Ribbons" of a Poly(Thiophene) Semiconductor. *ACS Nano* **2009**, *3*, 780.

(10) Diao, Y.; Shaw, L.; Bao, Z.; Mannsfeld, S. C. B. Morphology control strategies for solution-processed organic semiconductor thin films. *Energy Environ. Sci.* **2014**, *7*, 2145−2159.

(11) Diao, Y.; Zhou, Y.; Kurosawa, T.; Shaw, L.; Wang, C.; Park, S.; Guo, Y.; Reinspach, J. A.; Gu, K.; Gu, X.; Tee, B. C. K.; Pang, C.; Yan, H.; Zhao, D.; Toney, M. F.; Mannsfeld, S. C. B.; Bao, Z. Flow-enhanced solution printing of all-polymer solar cells. *Nat. Commun.* **2015**, *6*, 7955.

(12) Schott, S.; Gann, E.; Thomsen, L.; Jung, S.-H.; Lee, J.-K.; McNeill, C. R.; Sirringhaus, H. Charge-Transport Anisotropy in a Uniaxially Aligned Diketopyrrolopyrrole-Based Copolymer. *Adv. Mater.* **2015**, *27*, 7356.

(13) Bucella, S. G.; Luzio, A.; Gann, E.; Thomsen, L.; McNeill, C. R.; Pace, G.; Perinot, A.; Chen, Z.; Facchetti, A.; Caironi, M. Macroscopic and High-Throughput Printing of Aligned Nanostructured Polymer Semiconductors for MHz Large-Area Electronics. *Nat. Commun.* **2015**, *6*, 8394.

(14) Wang, G.; Huang, W.; Eastham, N. D.; Fabiano, S.; Manley, E. F.; Zeng, L.; Wang, B.; Zhang, X.; Chen, Z.; Li, R.; Chang, R. P. H.; Chen, L. X.; Bedzyk, M. J.; Melkonyan, F. S.; Facchetti, A.; Marks, T. J. Aggregation control in natural brush-printed conjugated polymer films and implications for enhancing charge transport. *Proc. Natl. Acad. Sci. U.S.A.* **2017**, *114*, No. E10066.

(15) Mohammadi, E.; Zhao, C.; Meng, Y.; Qu, G.; Zhang, F.; Zhao, X.; Mei, J.; Zuo, J.-M.; Shukla, D.; Diao, Y. Dynamic-template-directed multiscale assembly for large-area coating of highly-aligned conjugated polymer thin films. *Nat. Commun.* **2017**, *8*, 16070.

(16) Qu, G.; Zhao, X.; Newbloom, G. M.; Zhang, F.; Mohammadi, E.; Strzalka, J. W.; Pozzo, L. D.; Mei, J.; Diao, Y. Understanding Interfacial Alignment in Solution Coated Conjugated Polymer Thin Films. *ACS Appl. Mater. Interfaces* **2017**, *9*, 27863−27874.

(17) Zhang, F.; Mohammadi, E.; Luo, X.; Strzalka, J.; Mei, J.; Diao, Y. Critical Role of Surface Energy in Guiding Crystallization of Solution-Coated Conjugated Polymer Thin Films. *Langmuir* **2018**, *34*, 1109−1122.

(18) Gruber, M.; Jung, S.-H.; Schott, S.; Venkateshvaran, D.; Kronemeijer, A. J.; Andreasen, J. W.; McNeill, C. R.; Wong, W. W. H.; Shahid, M.; Heeney, M.; Lee, J.-K.; Sirringhaus, H. Enabling high-mobility, ambipolar charge-transport in a DPP-benzotriazole copolymer by side-chain engineering. *Chem. Sci.* **2015**, *6*, 6949−6960.

(19) Mei, J.; Diao, Y.; Appleton, A. L.; Fang, L.; Bao, Z. Integrated Materials Design of Organic Semiconductors for Field-Effect Transistors. *J. Am. Chem. Soc.* **2013**, *135*, 6724−6746.

(20) Chabinyc, M. L.; Lujan, R.; Endicott, F.; Toney, M. F.; McCulloch, I.; Heeney, M. Effects of the surface roughness of plastic-compatible inorganic dielectrics on polymeric thin film transistors. *Appl. Phys. Lett.* **2007**, *90*, 233508.

(21) Jung, Y.; Kline, R. J.; Fischer, D. A.; Lin, E. K.; Heeney, M.; McCulloch, I.; DeLongchamp, D. M. The Effect of Interfacial Roughness on the Thin Film Morphology and Charge Transport of High-Performance Polythiophenes. *Adv. Funct. Mater.* **2008**, *18*, 742−750.

(22) Tseng, H.-R.; Ying, L.; Hsu, B. B. Y.; Perez, L. A.; Takacs, C. J.; Bazan, G. C.; Heeger, A. J. High Mobility Field Effect Transistors Based on Macroscopically Oriented Regioregular Copolymers. *Nano Lett.* **2012**, *12*, 6353−6357.

(23) Tseng, H.-R.; Phan, H.; Luo, C.; Wang, M.; Perez, L. A.; Patel, S. N.; Ying, L.; Kramer, E. J.; Nguyen, T.-Q.; Bazan, G. C.; Heeger, A. J. High-Mobility Field-Effect Transistors Fabricated with Macroscopic Aligned Semiconducting Polymers. *Adv. Mater.* **2014**, *26*, 2993.

(24) Lee, W. H.; Cho, J. H.; Cho, K. Control of Mesoscale and Nanoscale Ordering of Organic Semiconductors at the Gate Dielectric/Semiconductor Interface for Organic Transistors. *J. Mater. Chem.* **2010**, *20*, 2549.

(25) Anglin, T. C.; Speros, J. C.; Massari, A. M. Interfacial Ring Orientation in Polythiophene Field-Effect Transistors on Functionalized Dielectrics. *J. Phys. Chem. C* **2011**, *115*, 16027−16036.

(26) Kim, D. H.; Park, Y. D.; Jang, Y.; Yang, H.; Kim, Y. H.; Han, J. I.; Moon, D. G.; Park, S.; Chang, T.; Chang, C.; Joo, M.; Ryu, C. Y.; Cho, K. Enhancement of Field-Effect Mobility Due to Surface-Mediated Molecular Ordering in Regioregular Polythiophene Thin Film Transistors. *Adv. Funct. Mater.* **2005**, *15*, 77−82.

(27) Kim, D. H.; Lee, H. S.; Shin, H.-J.; Bae, Y.-S.; Lee, K.-H.; Kim, S.-W.; Choi, D.; Choi, J.-Y. Graphene surface induced specific self-assembly of poly(3-hexylthiophene) for nanohybrid optoelectronics: from first-principles calculation to experimental characterizations. *Soft Matter* **2013**, *9*, 5355−5360.

(28) Müller, C.; Aghamohammadi, M.; Himmelberger, S.; Sonar, P.; Garriga, M.; Salleo, A.; Campoy-Quiles, M. One-Step Macroscopic Alignment of Conjugated Polymer Systems by Epitaxial Crystallization during Spin-Coating. *Adv. Funct. Mater.* **2013**, *23*, 2368−2377.

(29) Na, J. Y.; Kang, B.; Lee, S. G.; Cho, K.; Park, Y. D. Surface-Mediated Solidification of a Semiconducting Polymer during Time-Controlled Spin-Coating. *ACS Appl. Mater. Interfaces* **2017**, *9*, 9871−9879.

(30) Guo, D.-Y.; Tsai, Y.-b.; Yu, T.-F.; Lee, W.-Y. Interfacial effects on solution-sheared thin-film transistors. *J. Mater. Chem. C* **2018**, *6*, 12006−12015.

(31) Kim, C.; Facchetti, A.; Marks, T. J. Polymer Gate Dielectric Surface Viscoelasticity Modulates Pentacene Transistor Performance. *Science* **2007**, *318*, 76−80.

(32) Soeda, J.; Matsui, H.; Okamoto, T.; Osaka, I.; Takimiya, K.; Takeya, J. Highly Oriented Polymer Semiconductor Films Compressed at the Surface of Ionic Liquids for High-Performance Polymeric Organic Field-Effect Transistors. *Adv. Mater.* **2014**, *26*, 6430.

(33) Noh, J.; Jeong, S.; Lee, J.-Y. Ultrafast formation of air-processable and high-quality polymer films on an aqueous substrate. *Nat. Commun.* **2016**, *7*, 12374.

(34) Pandey, M.; Pandey, S. S.; Nagamatsu, S.; Hayase, S.; Takashima, W. Solvent driven performance in thin floating-films of PBTTT for organic field effect transistor: Role of macroscopic orientation. *Org. Electron.* **2017**, *43*, 240−246.

(35) Tripathi, A. S. M.; Pandey, M.; Sadakata, S.; Nagamatsu, S.; Takashima, W.; Hayase, S.; Pandey, S. S. Anisotropic charge transport

DOI: 10.1021/acsami.9b02923
ACS Appl. Mater. Interfaces 2019, 11, 22561−22574

in highly oriented films of semiconducting polymer prepared by ribbon-shaped floating film. *Appl. Phys. Lett.* **2018**, *112*, 123301.
(36) Wang, C.; Lee, W.-Y.; Kong, D.; Pfattner, R.; Schweicher, G.; Nakajima, R.; Lu, C.; Mei, J.; Lee, T. H.; Wu, H.-C.; Lopez, J.; Diao, Y.; Gu, X.; Himmelberger, S.; Niu, W.; Matthews, J. R.; He, M.; Salleo, A.; Nishi, Y.; Bao, Z. Significance of the double-layer capacitor effect in polar rubbery dielectrics and exceptionally stable low-voltage high transconductance organic transistors. *Sci. Rep.* **2015**, *5*, 17849.
(37) Cao, Y.; Morrissey, T. G.; Acome, E.; Allec, S. I.; Wong, B. M.; Keplinger, C.; Wang, C. A Transparent, Self-Healing, Highly Stretchable Ionic Conductor. *Adv. Mater.* **2017**, *29*, 1605099−n/a.
(38) Forrest, J. A.; Dalnoki-Veress, K. The glass transition in thin polymer films. *Adv. Colloid Interface Sci.* **2001**, *94*, 167−195.
(39) Fredlake, C. P.; Crosthwaite, J. M.; Hert, D. G.; Aki, S. N. V. K.; Brennecke, J. F. Thermophysical Properties of Imidazolium-Based Ionic Liquids. *J. Chem. Eng. Data* **2004**, *49*, 954−964.
(40) Tokuda, H.; Tsuzuki, S.; Susan, M. A. B. H.; Hayamizu, K.; Watanabe, M. How Ionic Are Room-Temperature Ionic Liquids? An Indicator of the Physicochemical Properties. *J. Phys. Chem. B* **2006**, *110*, 19593−19600.
(41) Fox, T. G. Influence of Diluent and of Copolymer Composition on the Glass Temperature of a Polymer System. *Bull. Am. Phys. Soc.* **1956**, *1*, 123−132.
(42) Forrest, J. A.; Dalnoki-Veress, K.; Stevens, J. R.; Dutcher, J. R. Effect of Free Surfaces on the Glass Transition Temperature of Thin Polymer Films. *Phys. Rev. Lett.* **1996**, *77*, 2002−2005.
(43) Höfft, O.; Bahr, S.; Kempter, V. Investigations with Infrared Spectroscopy on Films of the Ionic Liquid [EMIM]Tf2N. *Langmuir* **2008**, *24*, 11562−11566.
(44) Köhler, A.; dos Santos, D. A.; Beljonne, D.; Shuai, Z.; Brédas, J.-L.; Holmes, A. B.; Kraus, A.; Müllen, K.; Friend, R. H. Charge Separation in Localized and Delocalized Electronic States in Polymeric Semiconductors. *Nature* **1998**, *392*, 903.
(45) Vezie, M. S.; Few, S.; Meager, I.; Pieridou, G.; Dörling, B.; Ashraf, R. S.; Goñi, A. R.; Bronstein, H.; McCulloch, I.; Hayes, S. C.; Campoy-Quiles, M.; Nelson, J. Exploring the Origin of High Optical Absorption in Conjugated Polymers. *Nat. Mater.* **2016**, *15*, 746.
(46) Spano, F. C.; Silva, C. H- and J-Aggregate Behavior in Polymeric Semiconductors. *Annu. Rev. Phys. Chem.* **2014**, *65*, 477−500.
(47) Baker, J. L.; Jimison, L. H.; Mannsfeld, S.; Volkman, S.; Yin, S.; Subramanian, V.; Salleo, A.; Alivisatos, A. P.; Toney, M. F. Quantification of Thin Film Crystallographic Orientation Using X-ray Diffraction with an Area Detector. *Langmuir* **2010**, *26*, 9146−9151.
(48) Choi, H. H.; Cho, K.; Frisbie, C. D.; Sirringhaus, H.; Podzorov, V. Critical assessment of charge mobility extraction in FETs. *Nat Mater* **2018**, *17*, 2−7.
(49) Mei, J.; Kim, D. H.; Ayzner, A. L.; Toney, M. F.; Bao, Z. Siloxane-Terminated Solubilizing Side Chains: Bringing Conjugated Polymer Backbones Closer and Boosting Hole Mobilities in Thin-Film Transistors. *J. Am. Chem. Soc.* **2011**, *133*, 20130−20133.
(50) Sharma, A.; van Oost, F. W. A.; Kemerink, M.; Bobbert, P. A. Dimensionality of charge transport in organic field-effect transistors. *Phys. Rev. B: Condens. Matter Mater. Phys.* **2012**, *85*, 235302.
(51) Xue, G.; Zhao, X.; Qu, G.; Xu, T.; Gumyusenge, A.; Zhang, Z.; Zhao, Y.; Diao, Y.; Li, H.; Mei, J. Symmetry Breaking in Side Chains Leading to Mixed Orientations and Improved Charge Transport in Isoindigo-alt-Bithiophene Based Polymer Thin Films. *ACS Appl. Mater. Interfaces* **2017**, *9*, 25426−25433.
(52) Shaw, L.; Hayoz, P.; Diao, Y.; Reinspach, J. A.; To, J. W. F.; Toney, M. F.; Weitz, R. T.; Bao, Z. Direct Uniaxial Alignment of a Donor-Acceptor Semiconducting Polymer Using Single-Step Solution Shearing. *ACS Appl. Mater. Interfaces* **2016**, *8*, 9285.
(53) Lee, J.; Panzer, M. J.; He, Y.; Lodge, T. P.; Frisbie, C. D. Ion Gel Gated Polymer Thin-Film Transistors. *J. Am. Chem. Soc.* **2007**, *129*, 4532−4533.
(54) Cho, J. H.; Lee, J.; Xia, Y.; Kim, B.; He, Y.; Renn, M. J.; Lodge, T. P.; Daniel Frisbie, C. Printable ion-gel gate dielectrics for low-voltage polymer thin-film transistors on plastic. *Nat. Mater.* **2008**, *7*, 900.
(55) Cho, J. H.; Lee, J.; He, Y.; Kim, B. S.; Lodge, T. P.; Frisbie, C. D. High-Capacitance Ion Gel Gate Dielectrics with Faster Polarization Response Times for Organic Thin Film Transistors. *Adv. Mater.* **2008**, *20*, 686−690.
(56) Ono, S.; Miwa, K.; Seki, S.; Takeya, J. A comparative study of organic single-crystal transistors gated with various ionic-liquid electrolytes. *Appl. Phys. Lett.* **2009**, *94*, 063301.
(57) Zhang, S.; Lee, K. H.; Frisbie, C. D.; Lodge, T. P. Ionic Conductivity, Capacitance, and Viscoelastic Properties of Block Copolymer-Based Ion Gels. *Macromolecules* **2011**, *44*, 940−949.
(58) Qian, C.; Sun, J.; Yang, J.; Gao, Y. Flexible organic field-effect transistors on biodegradable cellulose paper with efficient reusable ion gel dielectrics. *RSC Adv.* **2015**, *5*, 14567−14574.
(59) Lee, J.; Kaake, L. G.; Cho, J. H.; Zhu, X.-Y.; Lodge, T. P.; Frisbie, C. D. Ion Gel-Gated Polymer Thin-Film Transistors: Operating Mechanism and Characterization of Gate Dielectric Capacitance, Switching Speed, and Stability. *J. Phys. Chem. C* **2009**, *113*, 8972−8981.
(60) Egginger, M.; Bauer, S.; Schwödiauer, R.; Neugebauer, H.; Sariciftci, N. S. Current versus gate voltage hysteresis in organic field effect transistors. *Monatshefte Chem. Chem. Mon.* **2009**, *140*, 735−750.
(61) Mulder, A.; Huskens, J.; Reinhoudt, D. N. Multivalency in supramolecular chemistry and nanofabrication. *Org. Biomol. Chem.* **2004**, *2*, 3409−3424.
(62) Huskens, J. Multivalent interactions at interfaces. *Curr. Opin. Chem. Biol.* **2006**, *10*, 537−543.
(63) Fasting, C.; Schalley, C. A.; Weber, M.; Seitz, O.; Hecht, S.; Koksch, B.; Dernedde, J.; Graf, C.; Knapp, E.-W.; Haag, R. Multivalency as a Chemical Organization and Action Principle. *Angew. Chem., Int. Ed.* **2012**, *51*, 10472−10498.
(64) Zhang, F.; Di, C.-a.; Berdunov, N.; Hu, Y.; Hu, Y.; Gao, X.; Meng, Q.; Sirringhaus, H.; Zhu, D. Ultrathin Film Organic Transistors: Precise Control of Semiconductor Thickness via Spin-Coating. *Adv. Mater.* **2013**, *25*, 1401−1407.
(65) Jiang, Z.; Li, X.; Strzalka, J.; Sprung, M.; Sun, T.; Sandy, A. R.; Narayanan, S.; Lee, D. R.; Wang, J. The dedicated high-resolution grazing-incidence X-ray scattering beamline 8-ID-E at the Advanced Photon Source. *J. Synchrotron Radiat.* **2012**, *19*, 627−636.
(66) Jiang, Z. GIXSGUI: a MATLAB toolbox for grazing-incidence X-ray scattering data visualization and reduction, and indexing of buried three-dimensional periodic nanostructured films. *J. Appl. Crystallogr.* **2015**, *48*, 917−926.
(67) Case, D. A.; Ben-Shalom, I. Y.; Brozell, S. R.; Cerutti, D. S.; Cheatham, T. E., III; Cruzeiro, V. W. D.; Darden, T. A.; Duke, R. E.; Ghoreishi, D.; Gilson, M. K.; Gohlke, H.; Goetz, A. W.; Greene, D.; Harris, R.; Homeyer, N.; Izadi, S.; Kovalenko, A.; Kurtzman, T.; Lee, T. S.; LeGrand, S.; Li, P.; Lin, C.; Liu, J.; Luchko, T.; Luo, R.; Mermelstein, D. J.; Merz, K. M.; Miao, Y.; Monard, G.; Nguyen, C.; Nguyen, H.; Omelyan, I.; Onufriev, A.; Pan, F.; Qi, R.; Roe, D. R.; Roitberg, A.; Sagui, C.; Schott-Verdugo, S.; Shen, J.; Simmerling, C. L.; Smith, J.; Salomon-Ferrer, R.; Swails, J.; Walker, R. C.; Wang, J.; Wei, H.; Wolf, R. M.; Wu, X.; Xiao, L.; York, D. M.; Kollman, P. A. *AMBER 2018*; University of California: San Francisco, 2018.
(68) Wang, J.; Wolf, R. M.; Caldwell, J. W.; Kollman, P. A.; Case, D. A. Development and testing of a general amber force field. *J. Comput. Chem.* **2004**, *25*, 1157−1174.
(69) Martínez, L.; Andrade, R.; Birgin, E. G.; Martínez, J. M. PACKMOL: A package for building initial configurations for molecular dynamics simulations. *J. Comput. Chem.* **2009**, *30*, 2157−2164.
(70) Schrödinger, L. *Schrödinger Release 2017-1: Maestro*; Schrödinger, LLC: New York, NY, 2017.

DOI: 10.1021/acsami.9b02923
ACS Appl. Mater. Interfaces 2019, 11, 22561−22574